Available online at www.sciencedirect.com
SCIENCE DIRECT®
Thin Solid Films 514 (2006) 110–119
thin solid films
www.elsevier.com/locate/tsf

X-ray diffraction analysis of the anisotropic nature of the structural imperfections in a sputter-deposited TiO_2/Ti_3Al bilayer

Y.H. Zhao [1], U. Welzel, J. van Lier, E.J. Mittemeijer *

Max Planck Institute for Metals Research, Heisenbergstr. 3, D-70569 Stuttgart, Germany

Received 6 July 2005; received in revised form 22 December 2005; accepted 20 February 2006
Available online 29 March 2006

Abstract

X-ray diffraction analysis was employed for the investigation of the structural imperfections of a sputter deposited TiO_2/Ti_3Al bilayer: The spatial distribution of crystallite size, microstrain and crystal orientation, as well as the strain-free lattice parameters, residual stresses and the Debye–Waller factor, were determined. The TiO_2 sublayer is largely amorphous. The Ti_3Al sublayer is polycrystalline and exhibits a pronouncedly anisotropic microstructure: It consists of columnar, needle-shaped crystallites with the crystal lattice *c*-axis as needle axis. The microstrain of the Ti_3Al-layer increases upon changing the viewing (diffraction vector) direction from vertical to parallel to the layer surface. The Ti_3Al layer is subjected to a large compressive macrostress parallel to the surface. The Debye–Waller parameter as determined for the Ti_3Al sublayer is larger than that of a reference Ti_3Al specimen. The investigations were complemented by transmission electron microscopy and energy-dispersive X-ray spectroscopy.

Keywords: Sputtering; X-ray diffraction; TiO_2/Ti_3Al bilayer; Microstructure; Crystallite size; Microstrain; Stress; Debye–Waller parameter

1. Introduction

Ti–Al alloys are promising structural materials because of their low mass density in combination with excellent mechanical properties at high temperatures [1]. However, they are susceptible to oxidation, which limits their high temperature application [2,3]. To obtain knowledge about the detailed oxidation process of Ti–Al alloys, oxide/metal bilayers (oxide = Al_2O_3, TiO_2, metal = TiAl, Ti_3Al, Ti) were prepared by sputter deposition as model systems. Recent investigations [4–6] revealed that upon annealing, oxides, in contact with the metallic Ti–Al layers, decompose; the released oxygen diffuses into the metallic layer and, also, a very thin layer of a new phase is formed at the interface. However, in other studies on the same oxide/metal system deviating observations on the interfacial reaction were made [7–11]. Such differences may well be caused by the different structural characteristics of the as-prepared thin layers, such as different amounts of structural imperfections (as grain boundaries and lattice mistakes), different internal stresses, etc. [12–15]. Hence, a detailed analysis of the characteristics of the microstructure of bi-(and) multilayers is of cardinal importance for understanding occurring phase transformations and interfacial reactions.

This paper presents a systematic investigation on the structural imperfections of in particular the Ti_3Al sublayer in a sputter-deposited TiO_2 (top)/Ti_3Al (bottom) bilayer system by applying different X-ray diffraction (XRD) techniques, complemented by transmission electron microscopy (TEM) and energy-dispersive X-ray spectroscopy (EDX). It is demonstrated that X-ray diffraction analysis is a versatile tool for quantitative microstructural investigation of the anisotropic nature of the microstructure: The spatial distribution of crystallite size, microstrain and crystal orientation, as well as the strain-free lattice parameters, residual stresses and the Debye–Waller factor, were determined.

* Corresponding author. Tel.: +49 711 689 3311.
E-mail address: e.j.mittemeijer@mf.mpg.de (E.J. Mittemeijer).
[1] On leave from the Shenyang National Laboratory for Materials Science, Institute of Metal Research, Chinese Academy of Sciences, Shenyang 110016, People's Republic of China; present address: Materials Science and Technology Division, Los Alamos National Laboratory, Los Alamos, NM-87545, USA.

0040-6090/$ - see front matter © 2006 Elsevier B.V. All rights reserved.
doi:10.1016/j.tsf.2006.02.076

2. Experimental details

2.1. Sample preparation

The TiO_2 (80 nm)/Ti_3Al (250 nm) bilayer specimen was deposited onto a mechanically polished single crystalline (111)-oriented Si substrate using a sputtering deposition system. The sputtering apparatus has four exchangeable targets, enabling the preparation of the TiO_2/Ti_3Al bilayer in the vacuum system in a single run. The base pressure of the sputtering system was typically below 2×10^{-5} Pa, and the working argon pressure was 2×10^{-1} Pa. A quartz crystal thickness monitor was used for calibration of the deposition rates. Before deposition the target and the substrate were sputter cleaned by argon ion sputtering. Then, a thin TiN buffer layer with a thickness of 50 nm was deposited on the Si substrate by reactive sputtering, to prevent reactions between the bilayer and the substrate. A 250 nm thick layer of Ti_3Al was then deposited onto the TiN buffer layer using a Ti_3Al target. Finally, an 80 nm thick TiO_2 layer was deposited by reactive sputtering. The deposition parameters have been given in Table 1.

A rectangular shaped sample (lateral dimensions of about 15 mm × 10 mm) cut from the specimen (wafer + bilayer) was used for the X-ray diffraction (XRD) measurements. For the preparation of a specimen for transmission electron microscopical (TEM) analysis, a small piece of the sample was subjected to standard specimen preparation techniques involving mechanical grinding, dimpling and Ar+ ion beam milling.

In order to prepare a reference specimen for the XRD line broadening investigations, a coarse-grained bulk specimen of Ti_3Al was prepared by melting of pure Ti (99.99 wt.%) and Al (99.999 wt.%) in an arc furnace under a pure Ar (99.999 wt.%) atmosphere. The bulk Ti_3Al alloy was ground into powder with particle size below 50 μm. The powder was then sealed in a small silica tube with 7×10^{4} Pa pure Ar and heat treated at 1273 K for 6 h to remove the structural imperfections.

2.2. X-ray diffraction (XRD) analyses

Philips X'Pert diffractometers (Philips Analytical, now Panalytical, Almelo, The Netherlands), equipped with Cu X-ray tubes operating at 1.8 kW were employed to perform phase analysis and to carry out texture, residual stress, crystallite size, microstrain and Debye–Waller parameter determinations. For phase analysis, a continuous θ–2θ scan from $2\theta = 10°$ to 125° (where 2θ is the diffraction angle) was carried out using a Philips X'Pert MPD diffractometer, equipped with a divergence slit (0.25°), an anti-scatter slit (0.25°), a receiving slit (0.10 mm) and a diffracted-beam graphite monochromator. For texture analysis, a Φ scan of the {002} reflection of the Ti_3Al sublayer was performed at different specimen tilt angles Ψ from 0 to 90° on a Philips X'Pert MRD diffractometer, where Ψ is the angle of inclination of the specimen surface normal with respect to the diffraction vector and Φ denotes the rotation of the specimen around the specimen surface normal. This diffractometer was equipped with a Eulerian cradle, an X-ray lens to achieve a parallel incident beam, a parallel plat-collimator placed in the diffracted beam and a diffracted-beam monochromator set to select Cu $K\alpha$ radiation. For determination of the crystallite size, the microstrain, the macro-(residual) stress and the Debye–Waller parameter, the {002}, {201}, {202}, etc., reflection peaks of the Ti_3Al layer, were recorded by θ–2θ scans at the selected tilt angles Ψ (see Section 4.3). XRD patterns of the Ti_3Al reference sample were recorded by a θ–2θ scan at $\Psi = 0°$.

Table 1
Deposition parameters of TiN, Ti_3Al and TiO_2 sub-layers

Thin layers	TiN	Ti_3Al	TiO_2
Partial pressure of O_2 (Pa)	–	–	5.7×10^{-2}
Partial pressure of N_2 (Pa)	4.5×10^{-2}	–	–
Deposition temperature (K)	<393	<373	<373
Deposition rates (nm/min)	13	9	8
Power on the target (kV × A)	1.9 × 0.9	1.7 × 0.6	1.7 × 0.6
Bias (V)	−40	–	–
Deposition time (min)	4	27	10

2.3. Transmission electron microscopy (TEM) and energy-dispersive X-ray analysis (EDX)

Cross-section TEM observations of the TiO_2/Ti_3Al bilayer were conducted on a JEOL 2000 FX electron microscope operated at 200 kV. Selected area diffraction patterns were taken with a camera length of 80 cm.

Local composition analysis of the TiO_2/Ti_3Al bilayer was performed in a JEOL Scanning Electron Microscope 6300F applying energy-dispersive X-ray (EDX) analysis. An acceleration voltage of 10 kV was used and the electron beam hit the specimen perpendicularly to the surface.

3. Data evaluation

Diffraction patterns were evaluated by fitting Pseudo–Voigt functions (for the definition of the profile function, see for instance Ref. [16]) using the Philips Analytical Profit 1.0c program (Philips Analytical, now Panalytical, Almelo, The Netherlands). A Pseudo–Voigt function is a weighted addition of a Gauss component and a Lorentz component. Peak positions ($2\theta_0$), heights (I_0), full widths at half maximum (FWHM) and shape parameters (η) were refined. The shape parameter η is defined as the Lorentz fraction of the Pseudo–Voigt function; $\eta = 0$ thus corresponds to a purely Gaussian peak profile, whereas $\eta = 1$ corresponds to a purely Lorentzian peak profile. The $K\alpha_2$ component was taken into account by simultaneous fitting of two Pseudo–Voigt functions, one for each radiation component. The FWHM and the shape parameters for the components were taken equal. A $K\alpha_2$/$K\alpha_1$ intensity ratio of 0.5 was assumed (this assumption was checked by setting the ratio free as a fit parameter for some evaluations). For each diffraction peak (or group of overlapping diffraction peaks), a linear background was fitted.

3.1. Peak broadening analysis

The measured diffraction profile $h(x)$ can be conceived as a convolution of an only structurally broadened profile $f(x)$ with the instrumentally broadened profile $g(x)$:

$$h(x) = f(x) \otimes g(x). \quad (1)$$

The structural line broadening can originate from small crystallite size and the microstrain due to dislocations, misfitting precipitates, etc. The instrumental broadening is due to the wavelength distribution, slit widths, etc. Both theory and experiment support that in many cases, the structurally broadened and the instrumentally broadened profiles can all well be approximated by Voigt functions (a Voigt function is the convolution of a Cauchy (Lorentz) function and a Gauss function). In this case, the integral breadths of the Gauss- and Cauchy components of the structurally broadened profiles, $\beta_{f,g}$ and $\beta_{f,c}$, respectively, can be obtained from the integral breadths (β_h) and the Voigt parameters (i.e., the ratio of the FWHM to the integral breadth) of the measured profiles (h) employing the so-called Voigt-method [17–19]. To this end, the integral breadths (β_g) and the Voigt parameters of the instrumentally broadened profiles (g) have to be known as well.

Assuming that the Cauchy component of the structurally broadened profile stems from the small crystallite size and that the Gauss component of the structurally broadened profile is due to microstrains, the crystallite size and the microstrain can be obtained from [19]:

$$\beta_{f,c} = \frac{K\lambda}{D\cos\theta_0}, \quad (2)$$

$$\beta_{f,g} = 4e\tan\theta_0, \quad (3)$$

where K is the Scherrer constant (taken equal to 1, i.e., the size value obtained is the volume-weighed domain size in the direction parallel to the diffraction vector). λ is the wavelength and θ_0 is the position of the diffraction line maximum. The value e is a measure for the microstrain (variation) in the specimen. For the case of a Gaussian strain distribution is it possible to calculate the local r.m.s. strain $\langle\varepsilon_0^2\rangle^{1/2}$ from e: $\langle\varepsilon_0^2\rangle^{1/2}=(2/\pi)^{1/2}e$ [18].

The single-line method described above is very useful to acquire a general understanding of origins of line broadening and to obtain estimates for crystallite size and microstrain. More accurate (and much more sophisticated) analyses of diffraction line broadening exist (see, for example, Ref. [20]), but such analyses exceed the scope of this work and are less appropriate here.

3.2. Peak position analysis

The 2θ-scale was calibrated by employing an external polycrystalline Si standard. In principle, the macrostress state of a crystalline specimen can be evaluated from the dependence of the (hkl) lattice spacing on (the rotation angle Φ and) the specimen tilt angle Ψ adopting the co-called $\sin^2\Psi$-method (see, for example, Refs. [21–23]). To this end, measured lattice strains for a particular reflection at a certain angle Ψ are usually plotted versus $\sin^2\Psi$. The components of the mechanical stress tensor can be determined from the slopes of straight lines (or the parameters of ellipses, for the case of shear stresses) by employing the so-called X-ray elastic constants. However, the method fails if the specimen is macroscopically elastically anisotropic due to texture and/or direction-dependent grain interaction. In such cases, a diffraction analysis of stresses is also possible using the so-called diffraction stress factors F_{ij}, which can be calculated after adopting a suitable grain-interaction model, employing the crystallographic orientation distribution function, if crystallographic texture occurs (see, for example, Refs. [22–26]). In many practical cases, however, the crystallographic texture of a specimen may be described in terms of one or a few so-called ideal orientations (crystallite groups), each consisting of crystallites all with the same crystallographic orientation (i.e., an ideal orientation is represented by a set of crystallographically equivalent points in Euler space). A method for diffraction stress analysis of such specimens with strong and sharp crystallographic texture components (i.e., the crystallographic orientation distribution function has a number of localised maxima in Euler space) was proposed by Willemse et al. [27] and Willemse and Naughton [28]. The method was adapted to rolled specimens by Hauk and Vaessen [29] (see also Refs. [30,31]). The crystallite group approach can, with certain restrictions, also be applied to fibre-textured specimens ([32]; for discussion of (also) limitations, see Ref. [33]).

For a fibre-textured specimen subjected to a biaxial, rotationally symmetric stress state ($\sigma_{11}=\sigma_{22}=\sigma_{\parallel}$, $\sigma_{12}=0$, $\sigma_{3i}=0$) consisting of hexagonal crystallites, it holds that [34]:

$$\varepsilon_\psi = \left[\left(s_{11}^* + s_{12}^* + 2s_{13}^*\right)\sin^2\Psi + 2s_{13}^*\right]\sigma_{\parallel} \quad (4)$$

where ε_ψ is the lattice strain measured at the tilt angle Ψ and s_{ij}^* are elastic compliances of the single crystal (in the single-crystal frame of reference). Eq. (4) implies that the lattice strain for each (hkl) plane relates linearly to $\sin^2\Psi$. Therefore, from the slope of a so-called $\sin^2\Psi$-plot (i.e., a plot of ε_ψ versus $\sin^2\Psi$), the stress value can be estimated if the value of $(s_{11}^*+ s_{12}^*+2s_{13}^*)$ is known.

Note that the measurement of the lattice strain of a crystallite group using a particular (hkl) reflection is not possible for all values of Ψ: As the diffraction vector is oriented perpendicular to the (hkl) planes to obtain diffracted intensity, an (hkl) reflection can only be found for certain combinations of Φ and Ψ, which are prescribed by the crystal structure of the material and the orientation of the crystallite group under investigation with respect to the specimen frame of reference. In this work, lattice strains obtained from different (hkl) reflections were combined in the stress analysis in order to obtain a meaningful linear regression [35].

3.3. Peak intensity analysis

For a flat-faced powder-briquette sample, symmetrically placed relative to the primary and diffracted beams, the power

per unit length of diffraction circle P' (i.e., the integrated intensity of a reflection recorded in a diffractometer with a given width of the receiving slit) is given by [36]:

$$P' = K(LP)mF_T^2 \tag{5}$$

where K represents the incident intensity multiplied by a set of physical constants, (LP) is the Lorentz-polarization factor and m and F_T are the multiplicity factor and the structure factor, respectively.

K is independent of the diffraction angle. L can be expressed for a given reflection at a Bragg reflection angle θ_0 as (see for example Refs. [36,37]):

$$L = (\sin\theta_0 \sin 2\theta_0)^{-1} \tag{6}$$

P allows for the partial polarization of the diffracted beam. When a crystal monochromator is used in the diffracted beam, the polarization factor can be represented as [37,38]:

$$P = \left(1 + \cos^2 2\alpha \cos^2 2\theta_0\right)/\left(1 + \cos^2 2\alpha\right) \tag{7}$$

where α is the Bragg angle of the crystal monochromator. The multiplicity factor is the number of equivalent reflections from a single crystal that are superimposed to form a powder line. F_T depends on the types of atoms in the unit cell and their relative positions (x_n, y_n, z_n) [39]:

$$F_T = \sum_n F_n e^{-M_n} = \sum_n f_n e^{-M_n} e^{2\pi i(hx_n + ky_n + lz_n)} \tag{8}$$

where $M_n = B_n \sin^2\theta/\lambda^2 = 8\pi^2 \langle u_n^2 \rangle \sin^2\theta/\lambda^2$, B_n is the Debye–Waller parameter, and $\langle u_n^2 \rangle$ is mean square atomic displacement of atoms n from their ideal lattice sites normal to the diffracting plane (hkl) [39]. f is the atomic scattering factor [40]:

$$f = f_0 + \Delta f' + i\Delta f'' \tag{9}$$

where f_0 is the uncorrected atomic scattering factor (see tables in Ref. [41]) and $\Delta f'$, $\Delta f''$ are the real and imaginary parts of the dispersion correction. The dispersion corrections depend on the X-ray wavelength and are less sensitive functions of θ than is f_0. The dispersion corrections are also tabulated [41]. When there is only one kind of atom in the unit cell, all M_n are the same [39]:

$$F_T^2 = F^2 e^{-2M} \tag{10}$$

Eq. (5) is valid only for an infinitely thick powder specimen (infinitely thick with respect to the penetration depth of the X-ray), for which the irradiated area always lies within the sample perimeter. For thin film specimens which are not infinitely thick as compared to the penetration depth (such as the currently investigated Ti_3Al thin layer with a thickness of 250 nm), the variation of the irradiated surface area and absorption with diffraction angle and specimen tilt angle have to be considered [42].

Eq. (5) is then changed to:

$$P' = K(LP)AGmF_T^2 \tag{11}$$

where A and G are the absorption factor and the geometrical factor (the illuminated area), respectively. For a homogeneous layer with thickness d, the absorption factor A can be given by [43,44]:

$$A = \tau - \tau \exp(-d/\tau) \tag{12}$$

here τ is the penetration depth and is given by [22]:

$$\tau = \sin\theta \cos\Psi / 2\mu_m \rho \tag{13}$$

where μ_m is the mass absorption coefficient of the material composing the sample, and ρ is the density of the sample. The illuminated area G of the sample is given by [43,44]:

$$G = G_0/\sin\theta\cos\Psi \tag{14}$$

where G_0 represents the cross section of the incident beam. Eq. (14) holds only if the illuminated area remains within the sample perimeter. When the sample thickness d is much larger than the penetration depth τ, the absorption factor A becomes equal to τ, and the product (AG) becomes θ and Ψ-independent (i.e., Eq. (5) holds).

Combining Eqs. (10) and (11), it follows that:

$$\ln\left[P'/\left(LPAGmF^2\right)\right] = \ln K - 2B(\sin\theta/\lambda)^2 \tag{15}$$

An average Debye–Waller parameter B can thus be determined from the slope of the straight line obtained by plotting $\ln[P'/(LPAGmF^2)]$ versus $(\sin\theta/\lambda)^2$.

In principle, the absorption and geometry correction described above can not be directly applied in the present case because the $Ti_3Al_{0.75}In_{0.25}$ layer was covered by a 80 nm thick TiO_2 layer. The intensity reduction due to absorption within the TiO_2 layer can be straightforwardly calculated (i.e., $I/I_0 = \exp(-d/\tau)$, where I/I_0 is the ratio of the intensities affected and unaffected by absorption, respectively). A calculation shows that the correction for absorption within the TiO_2 layer can be neglected due to the small thickness of the TiO_2 layer (note that only a correction for absorption in the TiO_2 layer, but no geometrical correction has to be applied).

The use of Eq. (15), in principle, relies on a flat-faced specimen being free of texture. For a textured specimen, the relative integrated intensities of the reflections are not only affected by the Debye–Waller factor but also depend on the texture state. Thus, they cannot be used without further ado for the determination of the Debye–Waller factor. The relative integrated intensities of the first- and second-orders of a Bragg reflection, however, are not affected by the texture and can thus be used to calculate the Debye–Waller factor B_{hkl} normal to the diffraction plane (hkl).

4. Results and discussion

4.1. Phase and texture analysis

A TEM bright-field cross-section image of the TiO_2/Ti_3Al bilayer is shown in Fig. 1a; the selected area electron diffraction patterns of the TiO_2 and Ti_3Al sub-layers are shown in Fig. 1b and c. The TiO_2 layer, of thickness 80 nm, appears to be

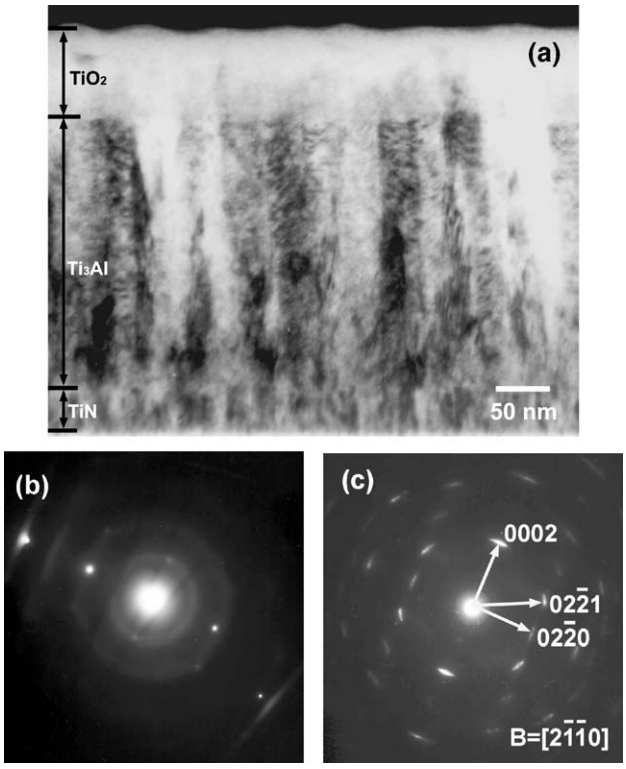

Fig. 1. (a) TEM bright-field cross-section image of the TiO_2/Ti_3Al bilayer. The TiO_2 layer is 80 nm thick. The polycrystalline Ti_3Al layer is 250 nm thick and composed of columnar grains. The TiN buffer layer is about 47 nm thick and is composed of very small columnar grains. (b) Selected area electron diffraction pattern of the TiO_2 sublayer; the broad halo and diffraction spots indicate that the TiO_2 sublayer is composed of both amorphous and crystalline phases. (c) Indexed electron diffraction pattern of the *hcp* Ti_3Al sublayer in the [2–1–10] beam direction.

composed of (mainly) amorphous and crystalline phases (see the amorphous halos and diffraction spots in Fig. 1b). The polycrystalline Ti_3Al layer, of thickness 250 nm, is composed of columnar grains and contains some nanometer-sized pores or voids within and/or between the grains. The diffraction contrast exhibited by the Ti_3Al columnar grains suggests that large stresses and/or defects occur within the grains. The Ti_3Al shows a strong texture (see Fig. 1c), as confirmed in particular by the XRD measurements discussed below. The TiN buffer layer is about 47 nm thick and is composed of very small columnar grains.

The XRD pattern of the TiO_2/Ti_3Al bilayer is shown in Fig. 2a. Apart from the 111, 222 and 333 reflections of the single crystalline Si substrate, two peaks are visible which are the 002 and 004 reflections of the Ti_3Al layer. No other peaks could be observed, also not upon detailed scanning of the diffraction angle range where peaks of crystalline TiO_2 and TiN are expected. The measured {002} pole figure of the Ti_3Al layer is shown in Fig. 2b. Clearly, the Ti_3Al layer exhibits a {001} fibre texture with the fibre axis perpendicular to the surface. These results suggest that the basal plane of the hexagonal closed packed crystal Ti_3Al, {001}, lies parallel to the surface of the bilayer/substrate. These results are consistent with the TEM observations (Fig. 1c).

4.2. Composition analysis

The energy-dispersive X-ray spectrum recorded in the scanning electron microscope from a surface of the $TiO_2/Ti_3Al/TiN/Si(111)$ bilayer is shown in Fig. 3. Besides elements Ti and Al from the sublayers, Si from the substrate (because the penetrating depth of the electron beam is about several micrometers) and a significant amount of indium were detected. The atomic concentrations of the as-prepared sample as obtained from the EDX-analysis have been listed in Table 2.

Because complete mutual solubility of the phases Ti_3Al and Ti_3In occurs [45], In can replace Al as a solute in the *hcp* Ti_3Al structure. From Table 2, assuming that In is distributed homogeneously in only the Ti_3Al sublayer, it follows that the atomic fraction of In in the Ti_3Al sublayer is 6.2 at.%, and the intermetallic phase can thus be indicated as $Ti_3Al_{0.75}In_{0.25}$. A Rutherford backscattering measurement performed in this work confirmed that about 6 at.% In was distributed homogeneously in the Ti_3Al layer.

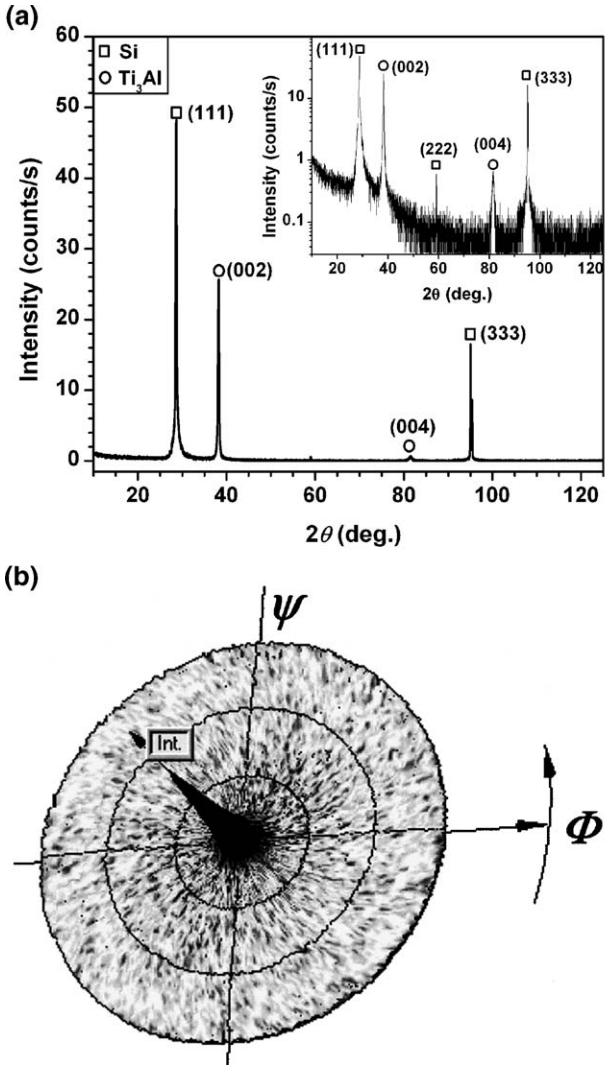

Fig. 2. (a) The XRD pattern of the TiO_2/Ti_3Al bilayer. The inset shows the same pattern with a logarithmic intensity scale. (b) {002} Pole figure of the Ti_3Al sublayer.

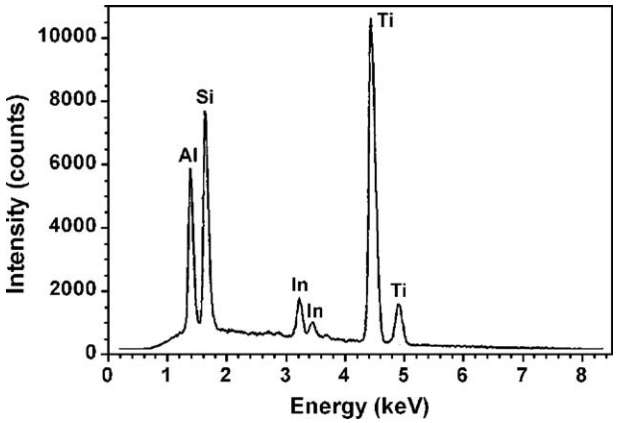

Fig. 3. Energy-dispersive X-ray spectrum of the $TiO_2/Ti_3Al/TiN/Si$ bilayer. Besides elements Ti and Al from the sublayers, In and Si (from the substrate) were detected.

The In content of the Ti_3Al is the result of In contamination of the target material employed in the sputter deposition. It is speculated that In sputters preferentially and as a consequence, a significant In concentration is detected in the deposited Ti_3Al layer.

4.3. Microstructure analysis

For the {001}-fibre-textured Ti_3Al layer (cf. Section 4.1), (*hkl*) diffraction peaks can be recorded only at particular Ψ angles. These Ψ angles for the crystallites with {001} planes parallel to the surface were calculated according to the unit cell structure of the crystalline Ti_3Al [46] (as shown in Fig. 4a) employing a stereographic projection; Fig. 4b shows the stereographic projection of fibre-textured Ti_3Al. In case of fibre-textured Ti_3Al, the poles form concentric circles. The Ψ angles for which the 001, 101, 102, 201 and 100 reflections can be recorded have been indicated in the schematic pole figure in Fig. 4b (for numerical values of the Ψ angles, see Table 3). Since a parallel beam geometry was employed for recording Bragg reflections under different tilting angles Ψ, the instrumental contribution to the diffraction line broadening is practically independent of the specimen tilt angle Ψ [44,47]. Thus, it is not necessary to record diffraction patterns of the reference sample at all specimen tilt angles Ψ employed in the analysis; a measurement at $\Psi=0°$ is sufficient.

4.3.1. Crystallite size and microstrain

The dependence of the profile-shape parameter η on the length of the diffraction vector ($\tau=4\pi \sin\theta/\lambda$) is shown in Fig. 5

Table 2
Atomic fractions of the $TiO_2/Ti_3Al/TiN/Si$ bilayer from the results of EDX-analysis

Element	Ti	Al	In
Atomic concentration (at.%)	81.6	13.7	4.7

The counting statistical errors of the concentration for elements Ti, Al, and In were below 0.4 at.%.

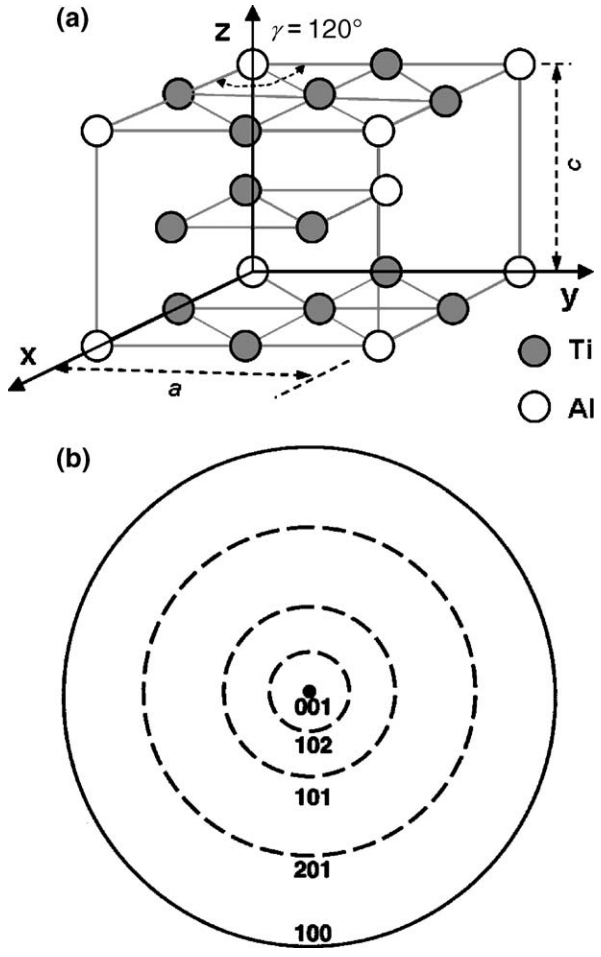

Fig. 4. (a) The ideal $D0_{19}$ structure of the hexagonal compound Ti_3Al. (b) Standard stereographic projection of the {001} fibre textured Ti_3Al layer. The poles form concentric circles (for a list of tilt angles, see Table 3).

for the Ti_3Al layer and the corresponding reference specimen. The XRD reflections of the Ti_3Al layer are largely of Lorentzian shape ($\eta>0.5$), whereas the XRD reflections of the reference sample are more of a Gaussian shape ($\eta<0.4$). Since both the only instrumentally broadened profiles measured from the Ti_3Al

Table 3
Crystallite, grain sizes *D* and microstrains *e*, derived from the diffraction line broadening for different *hkl* reflections; Ψ is the inclination angle between the {*hkl*} and the {001} planes

hkl	Ψ (°)	*D* (nm)	*e* (%)
002	0	52.2	0.24
201	61.67	9.3	0.64
202	42.84	8.9	0.94
203	31.73	12.4	0.49
222	58.09	9.3	0.75
401	74.91	7.3	0.77
004	0	40.0	0.26
402	61.67	4.5	0.79
403	78.48	6.0	0.55
421	20.35	9.6	0.85
224	38.77	8.6	0.32
205	51.04	16.1	0.40
422	67.83	8.1	0.74

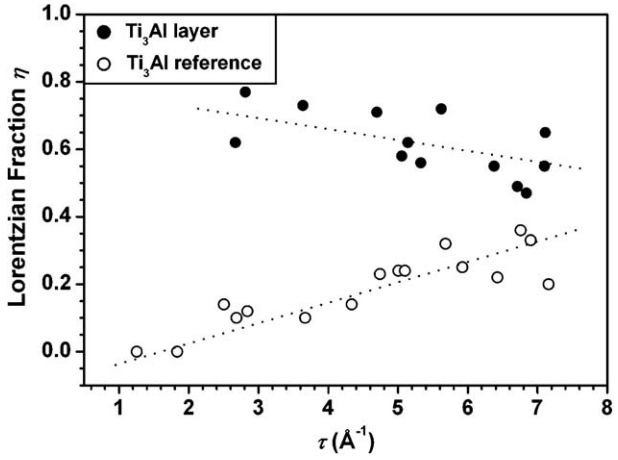

Fig. 5. The Lorentzian fractions η of the measured XRD profiles for the Ti_3Al layer and the reference sample versus the length of the diffraction vector ($\tau=4\pi\sin\theta/\lambda$).

reference and the structurally and instrumentally broadened profiles measured from the Ti_3Al layer can be well fitted by a Pseudo–Voigt function, the Voigt method [17–19] can be used to correct for the instrumental broadening and for the subsequent analysis of the grain size and microstrain of the Ti_3Al layer.

According to the Voigt method described in Section 3.1, the crystallite size D and microstrain e of the Ti_3Al layer have been calculated; the results have been listed in Table 3. Clearly, D and e exhibit anisotropic behaviours: the crystallite size along the <001> direction, D_{001}, is much larger than along the other directions, whereas e in the <001> direction is much smaller than along the other directions. To understand the anisotropic nature of D and e, D and e of the Ti_3Al layer were plotted against the tilt angle Ψ (see Fig. 6a and b).

With increasing Ψ from 0° to 80°, D decreases, initially sharply, from about 50 nm to about 6 nm. Recognising the columnar morphology of the Ti_3Al grains as observed by TEM (see Section 4.1), the Ψ-dependence of D can be well explained by the schematic figure shown in Fig. 6a. Assuming the Ti_3Al sublayer to be composed of rectangular grains with a height of 50 nm and a width of 6 nm, the crystallite (grain) size of the rectangular grain $D_{<hkl>}$*, as measured/viewed along the <*hkl*>* direction (i.e., along the diffraction vector, a vector in reciprocal space), can be written as 50 nm/cosψ for $0°<\Psi<6.89°$; 6 nm/sinψ for $6.89°<\Psi<90°$, as shown by the dotted line in Fig. 6a. The experimental data points agree well with the calculated dotted line.

The microstrain is a measure for the (variation of the) (local) lattice strains of the diffracting planes, which originate from microstresses caused by structural imperfections. According to Fig. 6b, the microstrain of the Ti_3Al layer increases approximate linearly with increasing Ψ. The amount of structural imperfection may be related to the grain size. Then the increase in microstrain with increasing ψ may be due to the decrease in grain size (or increase in grain boundary fraction) parallel to the direction of the diffraction vector with increasing Ψ. The grain boundary fraction F_{GB} can be related to grain size by [48]:

$$F_{GB} = g\Delta/D \tag{16}$$

where g is a geometrical constant and Δ is the grain boundary thickness. Taking g equal to 1 and Δ equal to 1.0 nm, the calculated grain boundary fraction variation against Ψ (using the data in Fig. 6a) has also been shown in Fig. 6b. The scatter in the F_{GB} data is caused by the scatter in the crystallite-size data as a function of tilt angle Ψ. The results suggest that, within experimental accuracy, F_{GB} and the microstrain indeed behave similarly as function of Ψ.

4.3.2. Lattice parameter and macrostress

From the fitting of the Pseudo–Voigt functions to the measured diffraction-line profiles, the lattice parameters of the Ti_3Al reference have been obtained from the peak maximum

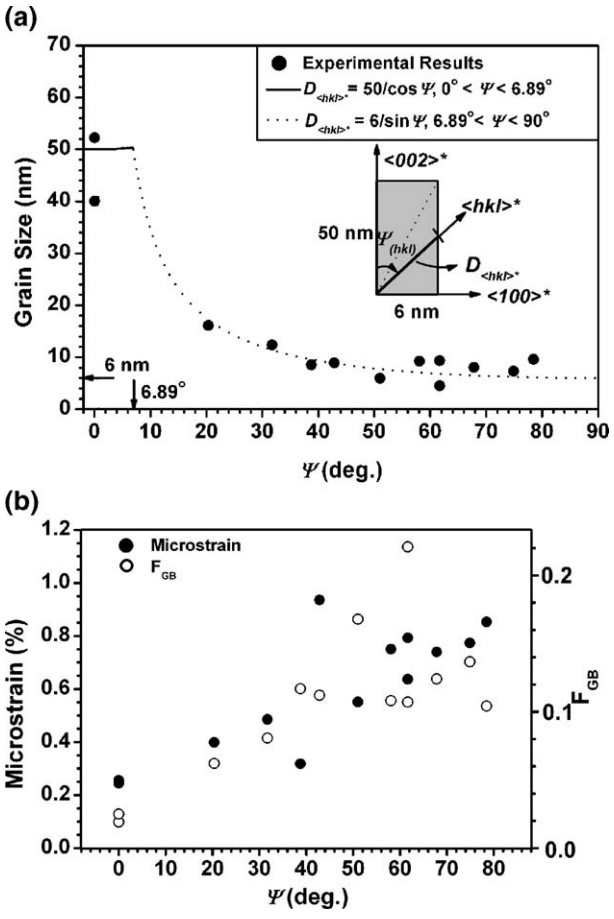

Fig. 6. (a) The crystallite, grain sizes of the Ti_3Al layer along different <*hkl*> directions against the tilting angle Ψ. The schematic figure represents the rectangular Ti_3Al grains (with a height of 50 nm and a width of 6 nm) in the Ti_3Al layer, the crystallite size of the rectangular grain $D_{<hkl>}$* measured along the <*hkl*>* direction was $50/\cos\Psi$ for $0°<\Psi<6.89°$; $6/\sin\Psi$ for $6.89°<\Psi<90°$, as shown by the solid and dashed lines. (b) The microstrains and the grain boundaries fraction F_{GB} of the Ti_3Al layer along different <*hkl*>* directions against the tilting angle Ψ. $F_{GB}=g\Delta/D$, where Δ is a constant relative to the grain boundaries' thickness, and equals 1.0 nm here [48]; g is a geometrical constant and equals 1.

Table 4
Measured and calculated values for the lattice parameters (a and c) and the axial ratio (c/a) of the $Ti_3Al_{0.75}In_{0.25}$ layer and the Ti_3Al reference, and literature values for Ti_3Al and Ti_3In

Sample	a (Å)	c (Å)	c/a
Ti_3Al reference (this work)	5.794±0.001	4.650±0.001	0.803
Ti_3Al [49]	5.797	4.648	0.802
Ti_3Al [50]	5.793	4.649	0.803
Ti_3In [45]	5.890	4.760	0.808
$Ti_3Al_{0.75}In_{0.25}$ (calculated)	5.819	4.678	0.804
Ti_3Al layer (measured)	5.808±0.001	4.697±0.002	0.809

using Bragg's law as $a=5.794\pm0.001$ Å, $c=4.650\pm0.001$ Å (see Table 4). These values agree well with the literature values: $a=5.797$ Å, $c=4.648$ Å [49] and $a=5.793$ Å, $c=4.649$ Å [50]. The measured lattice parameters of the $Ti_3Al_{0.75}In_{0.25}$ layer (the Ti_3Al layer contains about 6 at.% In; cf. Table 2) are $a=5.808\pm0.001$ Å, $c=4.6967\pm0.002$ Å, which are about 0.24% and 1.0% larger than the values of the reference Ti_3Al sample. The difference may be ascribed to the presence of In contamination (see Section 4.2) as a dissolved component in the Ti_3Al layer. If Vegard's rule holds, the lattice parameters of the $Ti_3Al_{1-x}In_x$ can be written as:

$$a_{Ti_3Al_{1-x}In_x} = a_{Ti_3Al} + (a_{Ti_3In} - a_{Ti_3Al})x \quad (17)$$

with the lattice parameters of Ti_3In as $a=5.890$ Å, $c=4.760$ Å [45]. The thus calculated value for the lattice parameter a of $Ti_3Al_{0.75}In_{0.25}$ is larger than the measured one of the $Ti_3Al_{0.75}In_{0.25}$ layer, and the thus calculated value for the lattice parameter c of $Ti_3Al_{0.75}In_{0.25}$ is much smaller than the measured one of the $Ti_3Al_{0.75}In_{0.25}$ layer, as listed in Table 4. Moreover, the axial ratio of c/a of the $Ti_3Al_{0.75}In_{0.25}$ layer (0.809) is about 0.62% larger than the calculated one of $Ti_3Al_{0.75}In_{0.25}$ (0.804). Recognising the very pronounced fibre texture, this result implies that the lattice spacing along the c-axis of the $Ti_3Al_{0.75}In_{0.25}$ layer (normal to the specimen surface) is enlarged and that the lattice spacing along the a-axis (parallel to the specimen surface) is compressed. This result suggests the occurrence of a biaxial compressive state of stress in the deposited $Ti_3Al_{0.75}In_{0.25}$ layer (see what follows).

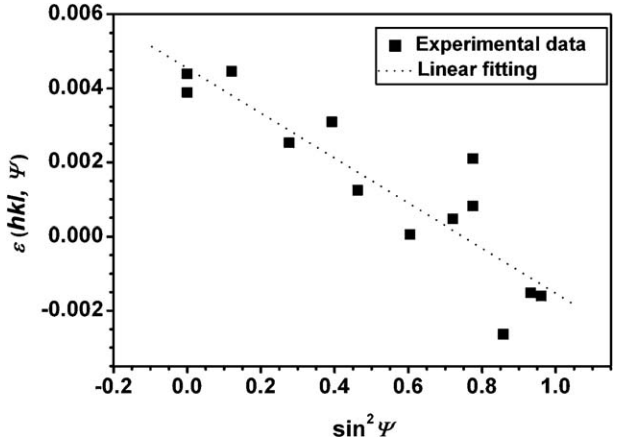

Fig. 7. The lattice strain of different (hkl) planes of the Ti_3Al layer $\varepsilon(hkl, \Psi)$ plotted versus $\sin^2\Psi$.

The lattice strain recorded for the (hkl) planes at tilt angle Ψ for the $Ti_3Al_{0.75}In_{0.25}$ layer, $\varepsilon(hkl, \Psi)$, can be calculated from the following equation:

$$\varepsilon(hkl, \Psi) = \frac{d(hkl, \psi) - d_0(hkl)}{d_0(hkl)} \quad (18)$$

where $d(hkl, \Psi)$ is the measured lattice spacing and $d_0(hkl)$ is the stress-free lattice spacing, which can be calculated from the theoretical values of the lattice parameters of $Ti_3Al_{0.75}In_{0.25}$ (cf. Eq. (12)). The thus obtained plot of the experimental data for $\varepsilon(hkl, \Psi)$ versus $\sin^2\Psi$ is shown in Fig. 7. Values for the elastic stiffnesses of the single crystal Ti_3Al at 270 K are: $c_{11}=176.2$ GPa, $c_{12}=87.8$ GPa, $c_{13}=61.2$ GPa, $c_{33}=218.7$ GPa, $c_{44}=62.4$ GPa, $c_{66}=44.2$ GPa [51]. With these values, the corresponding elastic compliances can be calculated: $s_{11}=7.83\times10^{-3}$ GPa^1, $s_{12}=-3.48\times10^{-3}$ GPa^1 and $s_{13}=-1.22\times10^{-3}$ GPa^1. $s_{33}=5.25\times10^{-3}$ GPa^1, $s_{44}=16.03\times10^{-3}$ GPa^1, $s_{66}=22.62\times10^{-3}$ GPa^1. Then, using Eq. (4), the residual stress of the Ti_3Al layer can be calculated from the slope of the straight line obtained by fitting to the data in the plot $\varepsilon(hkl, \Psi)$ versus $\sin^2\Psi$ as $\sigma_1=\sigma_2=-3.5$ GPa (see Fig. 7). For this analysis, it was presupposed that the stress state is rotationally symmetric. This presupposition seems reasonable considering the texture state (fibre symmetry).

The measured compressive macrostress is composed of two components: an extrinsic, thermal stress and an intrinsic, growth stress. The thermal stress develops upon cooling from the sputtering temperature $T_{sputtering}$ (=373 K) to room temperature T_{room} after layer growth and is due to the difference in the thermal expansion coefficients of the Ti_3Al and the Si substrate. Because the substrate is much thicker than the layer, it can be assumed that all thermal misfit is accommodated by the Ti_3Al layer. Then the thermal stress at the room temperature, σ_{th}, in the Ti_3Al layer can be calculated according to:

$$\sigma_{th} = \frac{E_{<Ti3Al>}}{1-\nu_{<Ti3Al>}}(\alpha_{<Si>} - \alpha_{<Ti3Al>})(T_{room} - T_{sputtering}) \quad (19)$$

where $\alpha_{<Ti3Al>}$ and $\alpha_{<Si>}$ are the linear coefficients of thermal expansion for Ti_3Al and c-Si, equal to 9.0×10^{-6} K^{-1} [52] and 2.6×10^{-6} K^{-1}, respectively [53]. $E_{<Ti3Al>}$ and ν are Young's modulus and Poisson's ratio of the Ti_3Al layer, which are equal to 144 GPa and 0.28, respectively [54]. Hence, σ_{th} (293 K) = 102.4 MPa and thus, the intrinsic growth stress is about −3.6 GPa. The intrinsic stress can be attributed to the effect of atomic peening occurring at low working gas (Ar) pressure during deposition, which can lead to the development of high residual compressive stresses in the growing layer [12–15].

4.3.3. Debye–Waller parameter

The Debye–Waller parameter can be obtained from the X-ray diffraction patterns by applying the method described in Section 3.3. Table 5 lists the values of the different terms in Eq.

Table 5
Peak positions $2\theta_0$, (LP) factors, multiplicity factors m, penetration depth τ, absorption factor A, geometrical factor G/G_0, dispersion-corrected atomic scattering factors of elements Al, Ti, In and solid solute $Al_{0.75}In_{0.25}$ (f_{Al}, f_{Ti}, f_{In} and $f_{Al0.75In0.25}$), structure factors of Ti_3Al and $Ti_3Al_{0.75}In_{0.25}$ (F^2_{Ti3Al} and $F^2_{Ti3Al0.75In0.25}$), measured values for the integrated intensity of XRD peaks P', ln ($P'G_0/LPAGmF^2$) and $\sin^2\theta/\lambda^2$ for the (002)–(004) reflection pair of the reference Ti_3Al and of the $Ti_3Al_{0.75}In_{0.25}$ layer

(hkl)	Ti_3Al reference		$Ti_3Al_{0.75}In_{0.25}$ layer	
	(002)	(004)	(002)	(004)
$2\theta_0$ (°)	38.82	83.31	38.20	81.51
LP	3.96	0.85	4.10	0.88
m	2	2	2	2
τ (10^{-4}cm)	–	–	1.98	3.96
A (10^{-4}cm)	–	–	0.235	0.242
G/G_0	–	–	3.056	1.532
f_{Al}	9.13	6.67	9.18	6.76
f_{Ti}	16.26	11.35	16.36	11.48
f_{In}	–	–	38.69	28.93
$f_{Al0.75In0.25}$	–	–	16.56	12.30
F^2_{Ti3Al}	13,407.71	6632.91	–	–
$F^2_{Ti3Al0.75In0.25}$	–	–	17,230.13	8,737.26
P' (arb. unit)	46,331	4400	672,732	30,768
$\ln(P'G_0/LPAGmF^2)$	−0.829	−0.941	11.102	10.895
$\sin^2\theta/\lambda^2$ (Å^2)	0.047	0.186	0.045	0.180

(15) for the (002)–(004) reflection pair of the Ti_3Al reference sample and the $Ti_3Al_{0.75}In_{0.25}$ thin sublayer.

The (LP) factor was calculated according to Eqs. (6) and (7). α is equal to 13.27 for the graphite monochromator used in the present work. Values for the mass absorption coefficient were taken from Ref. [41]. The density of $Ti_3Al_{0.75}In_{0.25}$ was taken as that of Ti_3Al (4.2 g cm^{-3} [46]). For the reference sample, because of the infinite thickness of the sample compared to the penetration depth, no correction for the variation of the irradiated surface area G and absorption factor A with diffraction angle has to be considered (cf. Section 3.3). The multiplicity factor is 2 for (002) and (004) reflections. For the calculation of the atomic scattering factors of the elements Al, Ti and In as functions of $\sin\theta/\lambda$, polynomial functions were fitted to f_0 data (taken from Ref. [41]). The atomic scattering factors f_{Al}, f_{Ti} and f_{In} corrected for dispersion (employing data from Ref. [41]) were then calculated from Eq. (9) (for results, see Table 5). The atomic scattering factor of the solid solute $Al_{0.75}In_{0.25}$, occurring at the Al sites in the Ti_3Al crystal structure, can be calculated by $f_{Al0.75In0.25}=0.75f_{Al}+0.25f_{In}$. The square of the structure factor can be represented by:

$$F^2=\left\{\sum_{j=1}^{n} f_j\cos 2\pi\left(hx_j+ky_j+lz_j\right)\right\}^2 + \left\{\sum_{j=1}^{n} f_j\sin 2\pi\left(hx_j+ky_j+lz_j\right)\right\}^2 \quad (20)$$

where j represents different atoms and/or the same atoms with different atomic positions in the unit cell. According to Fig. 4a, the unit cell of the hexagonal Ti_3Al contains 2 Al atoms in positions (0, 0, 0) and (2/3, 1/3, 1/2) and 6 Ti atoms in positions (1/2, 0, 0), (1, 1/2, 0), (1/2, 1/2, 0), (1/6, 1/3, 1/2), (1/6, 5/6, 1/2) and (2/3, 5/6, 1/2). Thus, F^2_{Ti3Al} can be calculated from f_{Al} and f_{Ti} and the atom positions in the unit cell (results in Table 5). Similarly, one can calculate $F^2_{Ti3Al0.75In0.25}$ by replacing f_{Al} with $f_{Al0.75In0.25}$ (see Table 5). Then using the experimentally determined integrated intensities, $\ln(P'G_0/(LPAGmF^2))$ and $\sin^2\theta/\lambda^2$ can be calculated.

Using the values of $\ln(P'G_0/LPAGmF^2)$ and $\sin^2\theta/\lambda^2$ listed in Table 5, one can calculate the Debye–Waller parameters along the <001> direction (B_{001}) for the reference Ti_3Al sample and the $Ti_3Al_{0.75}In_{0.25}$ layer using Eq. (11). B_{001} of the $Ti_3Al_{0.75}In_{0.25}$ layer is 0.76 Å^2, which is about twice the value obtained for the reference Ti_3Al sample ($B_{001}=0.40$ Å^2). It should be noted that the calculated Debye–Waller parameter represents an average for values of both Ti and Al(In) atoms. One cannot calculate the individual Debye–Waller parameters of Ti and Al(In) from the present data. The root mean square value of the atomic displacement, $\langle\mu^2\rangle^{1/2}$, can be calculated from the Debye–Waller parameter B using the relation $\langle\mu^2\rangle^{1/2}=(B/8\pi^2)^{1/2}$ [39]. $\langle\mu^2_{001}\rangle^{1/2}$ for the Ti_3Al layer thus is 0.10 Å, which equals about 3.4% of the nearest-neighbour spacing (2.856 Å). For the reference Ti_3Al sample, $\langle\mu^2_{001}\rangle^{1/2}$ is 0.07 Å which equals about 2.5% of the nearest-neighbour spacing.

The mean square root atomic displacement is composed of two contributions [55]: one is due to the thermal vibration of atoms (dynamic displacements). The other contribution is due to the static lattice distortions. The static atomic displacement is due to defects with displacement fields of essentially short range nature (see, for example, Ref. [56]), such as point defects (impurity atoms, vacancies, etc.). As discussed in Section 4.2, about 6 at.% In is dissolved in the Ti_3Al layer. Since the covalent radius of In (1.44 Å) is larger than those of Ti (1.32 Å) and Al (1.18 Å), dissolution of In in the Ti_3Al structure will cause static displacements of the surrounding atoms (Ti and Al) from their ideal lattice sites. It is concluded that the larger B parameter of the Ti_3Al layer as compared to the reference specimen is mainly caused by such static atomic displacements.

5. Summary

The structural imperfections of a sputter deposited TiO_2/Ti_3Al bilayer were characterized by means of XRD and TEM analyses. The TiO_2 layer is composed of amorphous and crystalline phases, and the Ti_3Al layer is polycrystalline, consisting of columnar-shaped grains with the crystal's lattice c-axis as column axis. About 6 at.% In is present in the Ti_3Al layer as a dissolved solute. A strong microstructural anisotropy exists. Upon changing the direction of the diffraction vector from vertical to parallel to the layer surface, the crystallite size decreases and the microstrain increases. These results can be conceived as a consequence of the columnar microstructure. A large compressive intrinsic growth stress (−3.6 GPa) prevails in the Ti_3Al layer. The Debye–Waller parameter of the Ti_3Al layer is larger than that of the reference Ti_3Al, which can be ascribed to static atomic displacements due to the presence of dissolved In.

References

[1] H.A. Lipsitt, Materials Research Society Symposium Proceedings, vol. 39, 1985, p. 351.
[2] G.H. Meier, Oxidation of High Temperature Intermetallics, TMS, Warrendale, PA, 1988, p. 1.
[3] G.H. Meier, Mater. Corros. 47 (1996) 595.
[4] A. Zalar, B. Baretzky, F. Dettenwanger, M. Rühle, P. Panjan, Surf. Interface Anal. 26 (1998) 861.
[5] A. Zalar, B. Baretzky, S. Hofmann, M. Rühle, P. Panjan, Thin Solid Films 352 (1999) 151.
[6] J. van Lier, B. Baretzky, A. Zalar, E.J. Mittemeijer, Surf. Interface Anal. 30 (2000) 124.
[7] Y.S. Chaug, N.J. Chou, H. Kim, J. Vac. Sci. Technol., A 5 (1987) 1288.
[8] H. Lefakis, M. Liehr, G.W. Rubloff, P.S. Ho, Materials Research Society Symposium Proceedings, vol. 54, 1986, p. 133.
[9] Y.C. Lu, S.L. Sass, Q. Bai, D.L. Kohlstedt, W.W. Gerberich, Acta Metall. Mater. 43 (1995) 31.
[10] Xin Chen, Youxiang Wang, Appl. Surf. Sci. 89 (1995) 169.
[11] J.H. Selverian, F.S. Ohuchi, M. Bortz, M.R. Notis, J. Mater. Sci. 26 (1991) 6300.
[12] M.F. Doerner, W.D. Nix, CRC Crit. Rev. Solid State Mater. Sci. 14 (1988) 225.
[13] J.A. Thornton, Thin Solid Films 171 (1989) 5.
[14] H. Windischmann, CRC Crit. Rev. Solid State Mater. Sci. 17 (1992) 547.
[15] R. Koch, J. Phys.: Condens. Matter 6 (1994) 9519.
[16] E.J. Sonneveld, R. Delhez, Th.H. de Keijser, E.J. Mittemeijer, Mat. Sci. Forum 79–82 (1991) 85.
[17] J.I. Langford, J. Appl. Crystallogr. 11 (1978) 10.
[18] J.I. Langford, R. Delhez, T.H. de Keijser, E.J. Mittemeijer, Aust. J. Phys. 41 (1988) 173.
[19] R. Delhez, Th.H. de Kejser, E.J. Mittemeijer, Fresenius Z. Anal. Chem. 312 (1982) 1.
[20] E.J. Mittemeijer, P. Scardi (Eds.), Diffraction Analysis of the Microstructure of Materials, Springer, Berlin, 2004.
[21] I.C. Noyan, J.B. Cohen, Residual Stress. Measurement by Diffraction and Interpretation, Spinger, New York, NY, 1987.
[22] V. Hauk, Structural and Residual Stress Analysis by Nondestructive Methods, Elsevier, Amsterdam, 1997.
[23] U. Welzel, J. Ligot, P. Lamparter, A.C. Vermeulen, E.J. Mittemeijer, J. Appl. Crystallogr. 38 (2005) 1.
[24] U. Welzel, E.J. Mittemeijer, J. Appl. Phys. 93 (2003) 9001.
[25] U. Welzel, M. Leoni, E.J. Mittemeijer, Philos. Mag. 83 (2003) 603.
[26] U. Welzel, M. Leoni, E.J. Mittemeijer, in: E.J. Mittemeijer, P. Scardi (Eds.), Diffraction Analysis of the Microstructure of Materials, Springer, Berlin, 2004, p. 363.
[27] P.F. Willemse, B.P. Naughton, C.A. Verbraak, Mater. Sci. Eng. 56 (1982) 25.
[28] P.F. Willemse, B.P. Naughton, Mater. Sci. Eng. 1 (1985) 41.
[29] V. Hauk, G. Vaessen, Z. Metallkd. 76 (1985) 102.
[30] V. Hauk, Adv. X-ray Anal. 29 (1986) 1.
[31] V. Hauk, R. Oudelhoven, Z. Metallkd. 79 (1988) 41.
[32] H.U. Baron, V. Hauk, Z. Metallkd. 79 (1988) 127.
[33] U. Welzel, E.J. Mittemeijer, Mat. Sci. Forum 443–444 (2004) 131.
[34] T. Hanabusa, K. Tominaga, H. Fujiwara, in: H. Fujiwara, T. Abe, K. Tanaka (Eds.), Residual Stresses: III. Science and Technology, vol. 1, Elsevier Applied Science, London, 1992, p. 728.
[35] A. Kumar, U. Welzel, E.J. Mittemeijer, in: R. Kuzel, E.J. Mittemeijer, U. Welzel (Eds.), European Powder Diffraction—Proceedings of EPDIC9, Z. Kristall. Supplement Issue, vol. 23, 2006, p. 55.
[36] B.E. Warren, X-ray Diffraction, Addison-Wesley, Reading MA, 1969, p. 49, chap. 4.
[37] R. Delhez, E.J. Mittemeijer, Th.H. de Keijser, H.C.F. Rozendaal, J. Phys. E: Sci. Instrum. 10 (1977) 784.
[38] L.V. Azaroff, Acta Crystallogr. 8 (1955) 701.
[39] B.E. Warren, X-ray Diffraction, Addison-Wesley, Reading, MA, 1969, p. 37, chap. 3.
[40] B.E. Warren, X-ray Diffraction, Addison-Wesley, Reading, MA, 1969, p. 11, chap. 1.
[41] C.H. Macgillavry, G.D. Rieck, International Tables for X-ray Crystallography, vol. III, Reidel, Dordrecht, 1983.
[42] H.J. Bunge, in: R.L. Snyder, J. Fiala, H.J. Bunge (Eds.), Defect and Microstructure Analysis by Diffraction, Oxford University Press, 1999, p. 460.
[43] H.J. Bunge, in: H.J. Bunge, C. Esling (Eds.), Quantitative Texture Analysis, Deutsche Gesellschaft für Metallkunde, Oberursel, 1982, p. 85.
[44] U. Welzel, M. Leoni, J. Appl. Crystallogr. 35 (2002) 196.
[45] K. Anderko, K. Sagel, U. Zwicker, Z. Metallkd. 48 (1957) 57.
[46] L. Christodoulou, in: R. Cahn (Ed.), Encyclopedia of Materials Science and Engineering, vol. 2, Pergamon, Oxford, 1992, p. 1346, Suppl.
[47] M. Leoni, U. Welzel, P. Scardi, J. Res. Natl. Inst. Stand. Technol. 109 (2004) 27.
[48] T. Mütschele, R. Kirchheim, Scr. Metall. 21 (1987) 1101.
[49] J. Braun, M. Ellner, Z. Metallkd. 91 (2000) 389.
[50] D. Clark, K.S. Jepson, G.I. Lewis, J. Inst. Met. 91 (1962–1963) 197.
[51] K. Tanaka, M. Koiwa, Intermetallics 4 (1996) S29.
[52] J. Kumpfert, Adv. Eng. Mater. 3 (2001) 851.
[53] R.B. Roberts, J. Phys. D: Appl. Phys. 14 (1981) L163.
[54] K. Tanaka, K. Okamoto, H. Inui, Y. Minonishi, M. Yamaguchi, M. Koiwa, Philos. Mag., A 73 (1996) 1475.
[55] M.A. Krivoglaz, Theory of X-ray and Thermal-Neutron Scattering by Real Crystals, Plenum, New York, 1969.
[56] T. Berger, A. Leineweber, E.J. Mittemeijer, P. Fischer, Phys. Status Solidi, A Appl. Res. 201 (2004) 1484.